

# Interfacial regulation with sodium-rich alloy/fluoride protective layer for reversible and dendrite-free sodium metal anodes

Megala Moorthy<sup>a</sup>, Ranjith Thangavel<sup>b</sup>, So Yeon An<sup>a</sup>, Hariharan Dhanasekaran<sup>a</sup>, Yun Sung Lee<sup>a,\*</sup>

<sup>a</sup> School of Chemical Engineering, Chonnam National University, Gwangju 61186, Republic of Korea

<sup>b</sup> Department of Chemical Engineering, Indian Institute of Technology Tirupati, Tirupati 517619, India

## ARTICLE INFO

### Keywords:

Sodium metal anode  
Sodium metal battery  
Artificial SEI layer  
Dendrite growth  
Symmetric cell  
Uniform deposition

## ABSTRACT

Sodium metal anode is heralded as a cornerstone for next-generation sodium battery technologies due to their low cost, high theoretical capacity, and elemental abundance. However, their practical deployment is hindered by the spontaneous formation of unstable heterogeneous solid electrolyte interphase (SEI), which induces uneven Na<sup>+</sup> deposition and uncontrolled dendrite growth. In this work, we report an ex-situ surface modification strategy using SnF<sub>2</sub> based solution, which reacts with sodium to form a Na<sub>15</sub>Sn<sub>4</sub>/NaF dual-phase artificial SEI layer. The Na<sub>15</sub>Sn<sub>4</sub> alloy acts as a sodio-philic and conductive scaffold to the Na surface, which promotes homogeneous Na<sup>+</sup> deposition and mitigating volume fluctuations. Meanwhile, the NaF component provides electronic insulation and mechanical reinforcement, effectively suppressing dendrite propagation. As a result, modified symmetric cells exhibit stable cycling for over 2000 hours with low overpotential, far outperforming pristine Na anode. The interlayer's effectiveness in dendrite suppression was also confirmed by in-situ optical microscopy. Furthermore, the Na<sub>15</sub>Sn<sub>4</sub> alloy/NaF (abbreviated as NS-a/NaF) anode delivers a high areal capacity (30 mAh cm<sup>-2</sup>), excellent rate capability (10 mA cm<sup>-2</sup>), and stable performance over 200 cycles at 1C in full cells paired with Na<sub>3</sub>V<sub>2</sub>(PO<sub>4</sub>)<sub>3</sub> cathode. This study presents a practical and scalable strategy for stabilizing sodium metal interfaces for high-performance rechargeable batteries.

## 1. Introduction

Over the past three decades, lithium-ion batteries (LIBs) have emerged as the dominant power source for modern electronic devices and electric vehicles (EVs), primarily due to their high energy density, long cycle life, and low self-discharge rate. These advantages have driven their widespread adoption across various applications, including large-scale energy storage systems (ESS) [1–3]. However, limited natural abundance of lithium, high cost of raw materials, and increasing sustainability concerns present significant obstacles to the large-scale, long-term deployment of LIBs. After more than a decade of intensive research, metallic sodium has gained widespread recognition as a leading candidate to replace lithium, particularly as a high-potential anode material for next-generation rechargeable batteries [4–6]. Metallic sodium, used directly as the anode in sodium metal batteries (SMBs), possesses several intrinsic properties that make its highly attractive, such as high theoretical specific capacity of 1166 mAh g<sup>-1</sup>,

low density (0.968 g cm<sup>-3</sup>), and a low standard electrochemical potential (−2.71 V vs. SHE). Compared to lithium-based systems, SMBs offer several techno-economic advantages, primarily arising from the natural abundance of sodium (~2.3 % Na vs. ~0.007 % for lithium in the Earth's crust) and significantly low raw material costs (approximately \$4/kg) [7–9]. These characteristics lay a strong foundation for the development of high-energy, cost-effective, and scalable sodium-based energy storage systems. Furthermore, sodium metal is actively being investigated in various advanced battery systems, including sodium–sulfur (Na–S) batteries [10], all-solid-state sodium batteries [11] and sodium–oxygen (Na–O<sub>2</sub>) batteries, [12] sodium carbon-dioxide (Na–CO<sub>2</sub>) batteries, [13] owing to its outstanding energy storage characteristics. Although sodium metal batteries are considered promising alternatives to lithium-based systems, their practical implementation is hindered by severe dendrite formation.

In particular, the direct use of sodium (Na) metal as an anode in batteries poses significant safety related challenges, due to its high

\* Corresponding author.

E-mail address: [leey@schoonnam.ac.kr](mailto:leey@schoonnam.ac.kr) (Y.S. Lee).

<https://doi.org/10.1016/j.surfin.2025.108323>

Received 21 August 2025; Received in revised form 24 November 2025; Accepted 12 December 2025

Available online 13 December 2025

2468-0230/© 2025 Elsevier B.V. All rights are reserved, including those for text and data mining, AI training, and similar technologies.

reactivity and thermodynamic instability, especially when in contact with organic electrolytes. They are generating a uneven, non-uniform heterogenous solid electrolyte interphase layer on the sodium metal surface [14,15]. These naturally generated SEI layer is ionically conductive and resists electron permeation, further preventing the electrolyte decomposition, but its spontaneous formation results in structural instability, which is further exacerbated during repeated sodium( $\text{Na}^+$ ) plating and stripping cycles. Over extended cycling, the unstable SEI cannot withstand the internal mechanical stress caused by non-uniform  $\text{Na}^+$  deposition, eventually leading to SEI rupture. Once its ruptured, the SEI develops numerous nanoscale defects and micro voids, exposing fresh sodium metal to the electrolyte over again. These newly exposed regions facilitate further uncontrolled electrochemical reactions, forming additional SEI layers in a self-reinforcing loop. The continuous SEI breakdown and regeneration not only consume electrolyte and active sodium, but also exacerbate dendrite growth in severe manner [16–18].

To address the persistent challenges associated with Na metal anodes, various strategies have been developed. These approaches including electrolyte modifications such as replacing new solvents, electrolyte composition modification, incorporation of high-electronegative additives to stabilize the SEI [19,20]. Several reports have already been published on three-dimensional (3D) structured host-type anodes, to improve the reversible plating/stripping behavior in lithium metal anodes [21–25]. Likewise, 3D current collector designs for sodium metal anodes, including carbon-based and highly conductive metal-based hosts with large specific surface areas and by reducing local current density it facilitates dendrite-free  $\text{Na}^+$  deposition [26,27]. However, the thickness of the host-type anode increases with the amount of sodium used during cycling, contributing to higher fabrication costs and larger overall battery sizes. In this context, interphase engineering emerges as a primary and cost-effective strategy for dendrite suppression. Recent studies have increasingly focused on developing artificial SEI layers with enhanced conductivity and mechanical strength to prevent dendrite formation.  $\text{Na}_3\text{Sb}$  [28],  $\text{Na}_3\text{P}$  [29],  $\text{NaF}$  [30],  $\text{NaCl}$  [31],  $\text{Na}_3\text{Bi}$  [32],  $\text{NaBr}$  [33],  $\text{Na-Bi}$  [32],  $\text{Na-Ga}$  [14], and  $\text{NaI}$  [34]. Moazzam Ali et al. designed a multifunctional ex-situ protective  $\text{MnSe/ZnSe@C}$  SEI layer. This hybrid structure offers several advantages, in-situ generated  $\text{Na}_2\text{Se}$  phase enhances uniform  $\text{Na}^+$  ion transport, Mn contributes to improving the mechanical robustness of the interlayer and Zn forms an alloy with Na, by introducing abundant sodio-philic sites that facilitate uniform nucleation and deposition [35]. To achieve a fast-charging and high-capacity operation, which is suitable for practical applications, it is critical to eliminate rugged electrode surfaces and develop interphases that simultaneously exhibit high ionic conductivity, low interfacial resistance, high mechanical robustness, and electronic insulation.

Herein, we report the successful formation of an artificial SEI composed of  $\text{Na}_{15}\text{Sn}_4$ , a sodium rich sodio-philic conductive alloy, and  $\text{NaF}$  electronically insulating phase, fabricated via a simple ex situ method involving the dissolution of  $\text{SnF}_2$  in dimethyl sulfoxide solvent. Other tin halide precursors ( $\text{SnCl}_2$  and  $\text{SnBr}_2$  in DMSO) were also evaluated, but they exhibited inferior electrochemical performance due to their lower mechanical integrity. Then, the symmetric cells incorporating the NS-a/ $\text{NaF}(\text{Na}_{15}\text{Sn}_4/\text{NaF})$  interphase demonstrated remarkable cycling stability ( $>2000$  hours), outstanding rate capability (up to  $10 \text{ mA cm}^{-2}$ ), and high areal capacity (up to  $30 \text{ mAh cm}^{-2}$ ), representing a significant advancement in sodium metal battery design. The interphase behavior of both pristine Na and NS-a/ $\text{NaF}$  was visually observed using optical microscopy. Furthermore, full cells paired with high-voltage  $\text{Na}_3\text{V}_2(\text{PO}_4)_3(\text{NVP})$  cathodes and either pristine or interphase-treated sodium anodes were evaluated. The NS-a/ $\text{NaF}$  anode delivered a high coulombic efficiency, high-rate capability, and excellent cycling stability maintaining reversible capacity of  $98 \text{ mAh g}^{-1}$  at 1C after 150 cycles. These results highlight that maintaining a stable artificial interphase via ex situ surface engineering offers a scalable, low-

cost strategy for suppressing dendrite formation and enabling the development of high-energy-density sodium metal batteries.

## 2. Experimental parts

### 2.1. Materials used for artificial SEI layer preparation

Absolute sodium metal cubes (99.99 %), tin fluoride ( $\text{SnF}_2$ , 99.99 %), tin chloride ( $\text{SnCl}_2$ , 99.99 %), tin bromide ( $\text{SnBr}_2$ , 99.99 %), from Sigma-Aldrich and dimethyl sulfoxide (DMSO) solvent sourced from Junesi Chemicals. Although the chemicals were supplied in anhydrous form, they were further dried by heating overnight and subsequently stored inside an argon-filled glove box to prevent moisture contamination. The commercial electrolyte, 1 M sodium hexafluorophosphate ( $\text{NaPF}_6$ ) in solvent (Diglyme), was purchased from Sigma-Aldrich and used for all electrochemical measurements.

### 2.2. Na metal foil preparation

Initially, sodium metal cubes were retrieved from a mineral oil container stored in an argon filled glove box. Subsequently, the sodium cubes were wiped with dry tissue paper to remove residual oil and laid over a thin plastic sheet. The oxidized surfaces and edges of the sodium cubes were then carefully cutted using a knife until the fresh sodium exposed. Following this, the resulting well-polished sodium metal was continuously rolled until a flat sodium foil is obtained, which was cut in to 12 mm discs and placed on a stainless-steel current collector for further processes.

### 2.3. Preparation of $\text{Na}_{15}\text{Sn}_4$ alloy/ $\text{NaF}$

To prepare the modified electrodes, 0.15 M anhydrous  $\text{SnF}_2$  solution was prepared by dissolving  $\text{SnF}_2$  in dissolving dimethyl sulfoxide solvent. The resulting solution was stirred for 4 hours to promote dissolution, and the resulting suspension was uniformly coated onto freshly polished sodium foil using a soft brush. Following the coating process, the sodium foil was vacuum dried for 6 hours to ensure complete evaporation of the solvent. The dried sodium foil was then punched into 12 mm diameter electrodes for electrochemical testing at room temperature. All synthesis steps were performed in an inert atmosphere to prevent oxidation.

### 2.4. Materials characterization

High-resolution X-ray diffraction (XRD, EMPyrean, PANalytical, equipped with a Pixel 3D detector) using a  $\text{Cu K}\alpha$  source (1.8 kW& Max 60 kV, 55 mA) and wavelength ( $\lambda=0.15405 \text{ nm}$ ) was performed to confirm the structural characteristics of the artificial SEI layers on the sodium metal anodes. Field-emission scanning electron microscopy (FESEM, S-4700, Hitachi, Japan) was employed to analyze the morphology, uniformity, and surface composition of the artificial SEI layer before and after cycling. Energy-dispersive X-ray spectroscopy (EDS) was coupled with FESEM for elemental analysis. The composition and oxidation states of the artificial SEI interphases were further confirmed by using high-vacuum X-ray photoelectron spectroscopy (XPS, Thermo Fisher Scientific, Al  $\text{K}\alpha$  radiation). Optical microscopy was performed using the MSTECH-MST5500B instrument. During  $\text{Na}^+$  plating, optical microscopy was used to investigate dendrite formation behavior in both cases. Plating/stripping studies for symmetric cells and charge/discharge studies for full-cell systems were conducted using a Wona-Tech battery cycler.

### 2.5. Electrochemical characterization

The coin cell (CR2032) was assembled in a glove box with an oxygen and moisture level of less than 0.1 ppm. Electrodes prepared from both

pristine Na and NS-a/NaF were utilized for symmetric cell and full-cell studies. For the symmetric cells, pristine Na||pristine Na and modified Na||modified Na configurations were tested. For full-cell fabrication,  $\text{Na}_3\text{V}_2(\text{PO}_4)_3$  (NVP, MTI Korea), served as the cathode, while either pristine Na or NS-a/NaF electrodes as the anode. The voltage window for full-cell testing was maintained between (2.5 to 3.8 V vs.  $\text{Na}^+$ ) and tested at low C rates to high C rates. The mass loading of the cathode is  $6 \text{ mg cm}^{-2}$ . The electrolyte used in these studies are 1 M  $\text{NaPF}_6$  in diglyme, and a polypropylene separator with a thickness of  $15 \mu\text{m}$  is employed. For symmetric cells,  $50 \mu\text{L}$  of electrolyte was used. In the full-cell configuration, pristine Na|| $\text{Na}_3\text{V}_2(\text{PO}_4)_3$  (NVP) and modified Na||NVP cells were assembled, using  $200 \mu\text{L}$  of electrolyte. The plating/stripping and charge/discharge characteristics of all electrodes were mentioned above evaluated using the Wona-Tech battery cyclers. Electrochemical impedance spectroscopy (EIS) measurements were conducted with an alternating potential of 10 mV across a frequency range from 200 kHz to 100 mHz. SEM images were captured under different electrodeposition conditions and after various cycling intervals, while XPS analysis was performed following multiple cycles using symmetric cell studies. LSV plots were measured from (−0.2 to 0.2 V window) and different temperatures EIS study (25–65 °C) using sodium symmetric cells at Biologic workstation. For all the studies, sodium samples were prepared inside the glove box, sealed in airtight containers with additional vacuum bags, and quickly transferred to the measurement chamber to avoid air exposure.

### 3. Results and discussion

(Fig. 1a) schematically illustrates the simple fabrication process for creating an artificial ionically conductive NS-a/NaF interphase, by manually coating a  $\text{SnF}_2$  solution on the sodium metal foil under an inert atmosphere. Specifically, 0.15 M  $\text{SnF}_2$  was dissolved in DMSO solvent at room temperature and stirred for 4 hours to ensure uniform dispersion. The resulting solution was then evenly coated onto the sodium metal surface using a soft brush. Then, the rapid chemical transformation is

visually confirmed by the instantaneous color change of the sodium surface, from silvery-white to black, indicating a highly exergonic reaction, further supported by its negative Gibbs free energy. For comparison, other tin halide precursors ( $\text{SnCl}_2$  and  $\text{SnBr}_2$ ) were prepared using the same procedure, and corresponding photographic images are provided in (Fig. S1). Upon contact with the sodium surface,  $\text{SnF}_2$  undergoes a spontaneous reduction, forming a composite of sodium-rich, sodio-philic, ionically conducting (Na–Sn) alloy, along with NaF insulating phase. The composite uniformly adheres to the sodium surface, establishing a robust interphase with high sodium wettability and excellent structural /thermodynamic stability. The Na–Sn alloy not only promotes rapid sodium-ion transport, but also enables uniform and dendrite-free sodium ion deposition beneath the engineered interphase. Meanwhile, the NaF phase, being an excellent electronic insulator, suppresses undesirable electron leakage into the electrolyte and their low  $\text{Na}^+$  diffusion barrier [36] contributes significantly to interfacial passivation. Compared to pristine sodium, this configuration markedly improves interfacial stability. The resulting artificial solid electrolyte interphase (SEI) is predominantly inorganic and tightly bound to the metallic sodium, resembling native SEIs formed in situ but with enhanced durability [37]. The exact crystal structure of the artificial SEI layer (NS-a/NaF) on sodium metal was analyzed using XRD, as shown in (Fig. 1b). The artificial SEI layer primarily comprises the sodium rich  $\text{Na}_{15}\text{Sn}_4$  alloy, crystalline phases on the sodium metal surface, matching with (PDF:031-1327 for  $\text{Na}_{15}\text{Sn}_4$ ) & (PDF: 022-0948 for Na). From the XRD results, it can be clear that the  $\text{SnF}_2$  powder completely transformed into  $\text{Na}_{15}\text{Sn}_4$  alloy, with NaF phase. Additionally, the XRD pattern exhibits a small hump at  $19^\circ$  (2 $\theta$ ), which is attributed to the Kapton film used to cover the sodium surface to prevent atmospheric contamination. Then, scanning electron microscopy study was taken to see their morphology (Fig. 1c). presents SEM images of pristine Na, showing a relatively smooth surface, without a protective interphase layer. The pristine Na electrode benefits significantly from the newly formed homogeneous  $\text{Na}_{15}\text{Sn}_4$ /NaF interphase layer, which provides effective surface protection and helps suppress dendrite formation

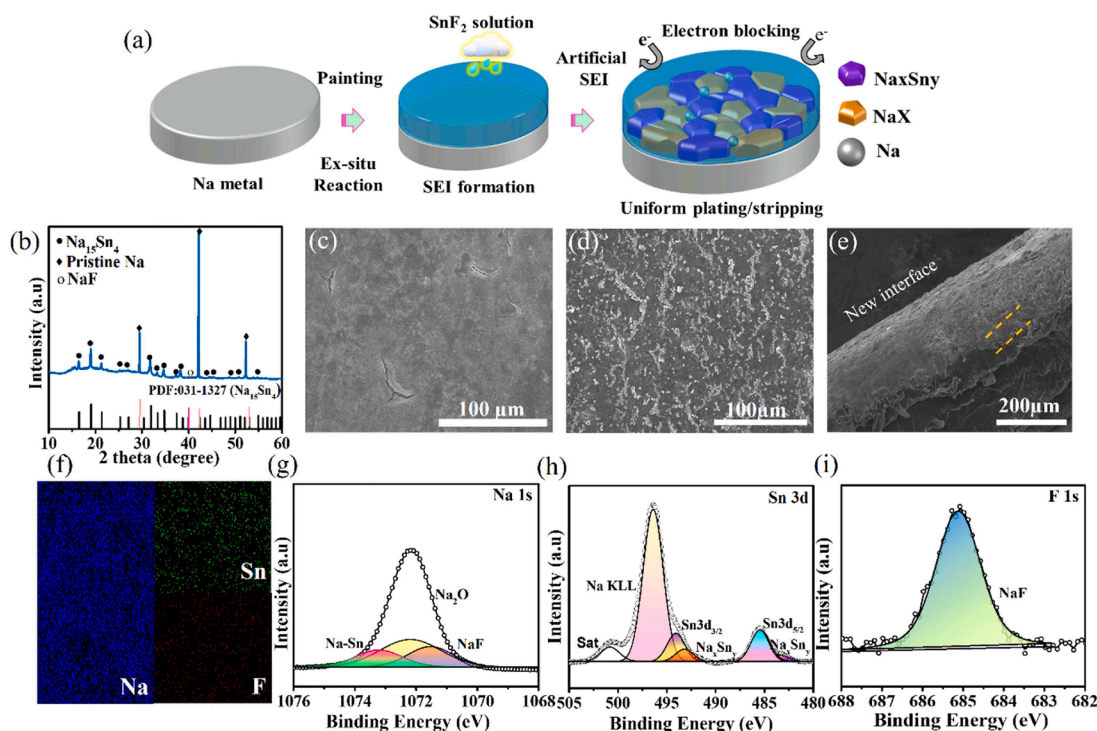


**Fig. 1.** a) Schematic representation of artificial interlayer fabrication on sodium metal. b) XRD pattern of new interlayer of NS-a/NaF modified anode. c) Surface SEM images of pristine Na and d-e) Surface and cross-sectional view of NS-a/NaF f) EDS mapping of the modified NS-a/NaF electrodes. g-i) High-resolution XPS spectra of Na 1s, Sn 3d, and F 1s.

(Fig. 1d) The cross-sectional SEM images of NS-a/NaF electrodes, revealing sheet-like structures uniformly covering the metal surface and thickness of the artificial SEI interphase was approximately 10  $\mu\text{m}$  (Fig. 1e). Additionally, (Fig. 1f) shows a uniform surface coating of  $\text{SnF}_2$ -derived particles on the sodium metal. Energy-dispersive X-ray spectroscopy (EDX) mapping further confirms the even distribution of Na, Sn, and F elements across the SEI layer. The homogeneous elemental dispersion across the surface provides strong evidence for the successful and uniform formation of the NS-a/NaF interphase. Furthermore, similar alloy interphases formed using  $\text{SnCl}_2$  and  $\text{SnBr}_2$  precursors are shown in (Fig. S2). In these cases, the sodium metal surfaces are fully covered by the respective interphase compositions.

The formation of new NS-a/NaF interphases chemical composition, oxidation states were further confirmed by high-vacuum X-ray photoelectron spectroscopy (XPS). These NS-a/NaF SEI on the sodium metal surface promote faster  $\text{Na}^+$  ion transport and uniform sodium ion deposition beneath it. When sodium ions encounter the pre-formed artificial interphase, a minimal amount of organic SEI, typically formed from electrolyte decomposition, remains unreactive and does not obstruct access to sodium metal. In contrast, the ionically conductive  $\text{Na}_{15}\text{Sn}_4$  alloy and insulating NaF phase form directly adjacent to the sodium metal anode, creating a functional and stable interphase. The Na 1 s spectra exhibits a peak at 1073.3, 1071.5 eV, corresponding to the formation of  $\text{Na}_{15}\text{Sn}_4$  & NaF and the peak at 1072.1 eV is attributed to the oxidation reaction ( $\text{Na}_2\text{O}$ ) during the sample transfer as shown in (Fig. 1g). The peak at 500.9 eV corresponds to a satellite feature, while the Na KLL peak overlaps with the Sn 3d spectrum [38,39]. The Sn 3d spectrum were fitted into two positions at 493.9 eV and 485.3 eV, corresponding to Sn  $3d_{3/2}$  and Sn  $3d_{5/2}$ , respectively. In addition, the peak observed at 493.02 eV, 483.1 eV is attributed to Na-Sn alloy phases, [40] as shown in (Fig. 1h). Additionally, the F 1 s spectrum at 685.45 eV, confirming the presence of NaF phases (Fig. 1i). Together, Na 1 s, Sn 3d,

and F 1 s spectra confirm the existence of the  $\text{Na}_{15}\text{Sn}_4$  alloy and NaF phases on the sodium metal surface. These interphases are responsible for reducing the ion migration barrier near the metal anode, thereby lowering both the nucleation and growth overpotentials during the plating/stripping process.

Fig. 2a schematically compares the plating/stripping behavior of pristine sodium metal and artificial SEI layer (NS-a/NaF)-protected sodium metal. In the absence of a protective interphase (top row), repeated cycling leads to non-uniform  $\text{Na}^+$  deposition, causing dendritic growth and ultimately provides the unstable cell performance. In contrast, when a uniform NS-a/NaF layer is applied onto the sodium surface via a simple coating method (bottom row), it forms a robust and stable interfaces. Thus enables homogeneous sodium-ion flux, thereby facilitating uniform plating/stripping and effectively suppressing dendrite formation. Further, to evaluate the superiority of the prepared NS-a/NaF interphase electrodes in enhancing  $\text{Na}^+$  storage and improving electrochemical performance, a series of symmetric cells, and full cells were assembled using 1 M  $\text{NaPF}_6$  in diglyme electrolyte. As shown in (Fig. 2b). In a representative test, 1  $\text{mAh cm}^{-2}$  of  $\text{Na}^+$  was galvanostatically plated at a current density of 1  $\text{mA cm}^{-2}$ . The pristine sodium electrode displayed a pronounced nucleation overpotential of 20 mV and growth overpotential of 25 mV, indicative of sluggish  $\text{Na}^+$  diffusion and poor interfacial wettability. In contrast, the NS-a/NaF-modified electrode exhibited markedly reduced nucleation (11 mV) and growth (15 mV) overpotentials, this indicates that the ionically conductive  $\text{Na}_{15}\text{Sn}_4/\text{NaF}$  interphase not only facilitates rapid  $\text{Na}^+$  diffusion into the SEI, but also exhibits strong sodium affinity, resulting in more efficient and uniform sodium deposition as shown in (Fig. 2c). Furthermore, to validate the underlying mechanism and effectiveness of the NS-a/NaF artificial interphase, symmetric cells were galvanostatically cycled at 2  $\text{mA cm}^{-2}$ , with an areal capacity of 2  $\text{mAh cm}^{-2}$ , as shown in (Fig. 2d). The as-prepared NS-a/NaF-modified sodium anode

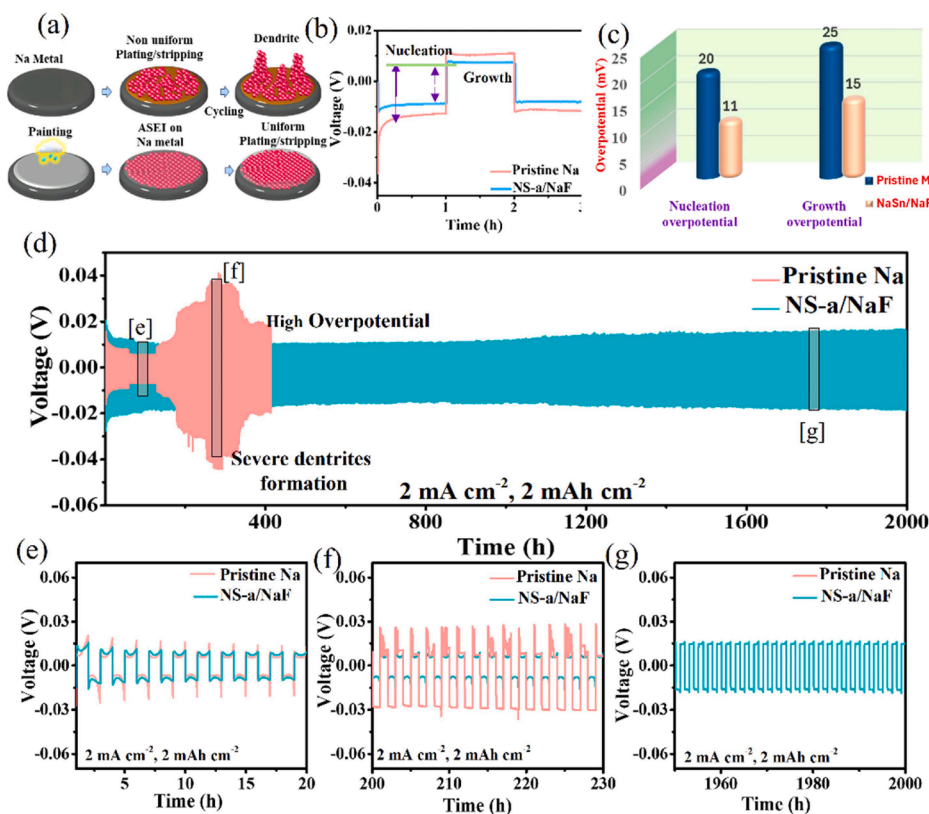


**Fig. 2.** Interphase behavior analysis. a) Scheme highlighting the protective layer coating with and without the interlayer, showing how dendrites are formed. b&c) Nucleation and growth overpotential of NS-a/NaF and pristine Na electrodes. d) Plating/stripping profile at 2  $\text{mA cm}^{-2}$  and 2  $\text{mAh cm}^{-2}$  areal capacity. e-g) Enlarged plating/stripping profiles of both electrodes.

exhibited exceptionally low overpotential and smooth, stable plating/stripping behavior from the initial cycles, attributable to the high-quality artificial SEI layer formed via a controlled ex situ reaction on the sodium surface. The NS-a/NaF anode achieved remarkable stability, maintaining consistent plating/stripping for up to 2000 h with a flat and uniform voltage profile. This indicates that the rate of reaction could be enhanced in NS-a/NaF interphase, as well as new organic SEI from the electrolyte formed during the cycling, which also contributes extra protection to the sodium metal. It is worth noting that the enhanced chemical and electrochemical properties of the artificial NS-a/NaF only enable more uniform sodium plating and stripping.

In addition, to support the superiority of the NS-a/NaF interlayer, its ionic transport behavior was evaluated using electrochemical impedance spectroscopy (EIS) with a separate cell setup, as shown in (Fig. S3). Based on the equation, the calculated ionic conductivity of the NS-a/NaF interlayer was  $5.86 \text{ mS cm}^{-1}$ , confirming efficient  $\text{Na}^+$  transport through the interphase [29]. Additionally, the exceptional cycling stability observed with the NS-a/NaF electrode is primarily attributed to the excellent mechanical robustness of the interphase, which plays a crucial role in sustaining long-term cycling performance. In contrast, pristine Na metal electrode with naturally derived SEI without the proper protection, exhibited severe voltage fluctuations, non-uniform sodium ion deposition and dissolution during the plating/stripping process. Although the pristine Na anode remained relatively stable during the initial cycles due to the naturally formed SEI layer, a sudden voltage drop was observed after 55 h of plating/stripping. Because interphase side reactions increased as time progressed, loose SEI layers became permeable to electrolyte ions. These type of reactions facilitate the dendrite formation, easy to conduct the dendrite again, resulting in high overpotential, high impedance, and eventual cell failure [41–43]. Further analysis of the voltage vs time profile as shown in (Fig. 2e–g) the pristine Na anode exhibited an initial overpotential of 17 mV. However, due to dendrite proliferation, the voltage dropped and fluctuated continuously. Later, the overpotential sharply jumped to 70 mV, after 289 hours and again dropped, later the cell dead, no more active. In contrast, the NS-a/NaF anode demonstrated a much lower initial growth potential of 16 mV with voltage spikes, which increased to 20 mV after 100 hours and maintained until the cell dead. In the early cycles, the NS-a/NaF interface shows slight voltage spikes due to an immature artificial SEI and uneven sodium nucleation. Over time, the interface self-reconstructs, improving contact, ion transport, and promoting uniform  $\text{Na}^+$  deposition.

Furthermore, the thickness of the newly formed artificial NS-a/NaF layer on sodium metal is another crucial factor, that significantly influences the long-term cycling stability. To quantify this effect, the SEI thickness was analyzed for samples prepared using different solution concentrations. Specifically, 0.1 M, 0.15 M, and 0.25 M concentrations were prepared, representing low, medium, and high concentration levels, respectively. The corresponding alloy solutions were coated onto sodium metal anodes and dried for 5 hours. Subsequently, the symmetric cell performance of all concentration-based electrodes was evaluated. Among them, the 0.1 M sodium symmetric cell exhibited uneven plating/stripping behavior up to 200 hours, accompanied by a high overpotential. This instability arises from an un-stable artificial SEI layer, which fails to effectively protect the sodium metal from direct electron transfer reactions. In comparison, the 0.25 M electrode showed stable cycling for only about 50 hours, primarily due to its high charge-transfer resistance. The use of highly concentrated solutions results in the formation of thick interlayers that hinder long-term cycling stability. Between these two combinations, 0.15 M concentration was found to be optimal, facilitating uniform plating/stripping with a low overpotential [44]. The optimized interlayer likely possesses a uniform and compact interphase compared to the other concentrations. In addition, post-cycling EIS analysis further confirmed that the charge-transfer resistance of the different variations. Both 0.1 M and 0.25 M samples are higher than that of the optimized 0.15 M sample (Fig.S4). As shown

in (Fig.S5 a), our rationally designed NS-a/NaF electrodes, featuring robust interphases, successfully suppress dead  $\text{Na}^+$  accumulation and dendrite growth, ultimately delivering superior rate performance compared to previously reported results (Table- [29,45–54]). Furthermore, electrochemical impedance spectroscopy (EIS) was employed to evaluate the interfacial stability and reaction kinetics of both the NS-a/NaF and pristine Na electrodes using symmetric cells. The interphase resistance of pristine Na and NS-a/NaF anodes, before and after extended cycling (post-mortem analysis-50,100,200 cycles), is presented in (Fig. S5 b&c). In the case of pristine sodium, the charge-transfer resistance is initially low before cycling, which can be attributed to the presence of a naturally formed solid electrolyte interphase [55] layer. However, as cycling progresses, this unstable SEI layer fails to maintain uniform nucleation due to its heterogeneous nature. Consequently, pristine Na experiences several issues such as mechanical stress and dendrite growth. These dendrites eventually puncture the SEI layer, making ion transport across the interface highly inefficient, which leads to a continuous increase in resistance with further cycling of 50, 100, 200. In contrast, the NS-a/NaF interphase exhibits a much lower charge-transfer resistance. Even after prolonged cycling, it retains its structural integrity of artificial interlayer, resulting in only a slight unavoidable increase in resistance, less than that observed in pristine sodium [56]. Then, for the comparison purposes, the rest of the other Sn halogenated interphases on sodium metal, their plating/stripping is validated using the symmetric cell performance. Unfortunately, even though they are electrochemically stable interphases, due to their low mechanical strength, they failed to achieve the long-term cycling performance as shown in (Fig. S6). After 100 cycles of plating and stripping, both symmetric cells were disassembled to visually examine the electrodes. On the pristine Na electrode, obvious side reactions were visible to the naked eye on both the plated and stripped sides, indicating surface degradation (Fig. S7a). In contrast, the NS-a/NaF electrode appeared much cleaner, suggesting better surface stability. These observations were further supported by cross-sectional SEM images (Fig. S7b), where the pristine Na showed a rough and uneven surface, while the NS-a/NaF electrode maintained a smoother and more compact morphology, in which clear evidence of the protective effect offered by the artificial SEI layer.

To further evaluate the interfacial behavior and morphological evolution of the pristine Na metal anode and NS-a/NaF artificial SEI-coated anode, ex situ SEM analysis was performed. The uniform structure of the interphase layer plays a critical role in guiding even sodium-ion deposition, which helps suppress dendrite formation and significantly enhances the overall cycling performance. To examine this, a controlled amount of  $\text{Na}^+$  ions was galvanostatically deposited and stripped on the electrode surfaces for 25 cycles, with the process halted at the final plating step. The cells were then immediately dismantled, rinsed with electrolyte, and dried to observe the resulting surface morphology. At a low areal capacity of  $5 \text{ mAh cm}^{-2}$ , low current density of  $2 \text{ mA cm}^{-2}$ , sodium ion deposition is minimal, resulting in a NS-a/NaF protective layer is covered uniformly. As the areal capacity increases to  $10 \text{ mAh cm}^{-2}$ , more amount of sodium ions get deposited beneath the SEI layers. The newly formed NS-a/NaF artificial SEI layer, characterized by high ionic conductivity, effectively regulates uniform sodium ion deposition and maintains structural integrity despite the volume changes associated with high deposition [57,58]. While some surface changes are less noticeable at this higher capacity, but the deposition surface looks smooth, thus NS-a/NaF layer effectively protects them from unwanted parasite reactions. At an even higher areal capacity increased to  $30 \text{ mAh cm}^{-2}$  increased sodium ion deposition leads to the, formation of thickened  $\text{Na}^+$  deposition layers at localized regions. However, the SEI layers continue to promote homogeneous deposition and delay dendrite formation without cracks over Na metal anode [59]. The newly formed NS-a/NaF anode demonstrates enhanced uniformity, which is the most important criteria for the interphase type anodes as shown in (Fig. 3) In contrast, the morphology of pristine Na under

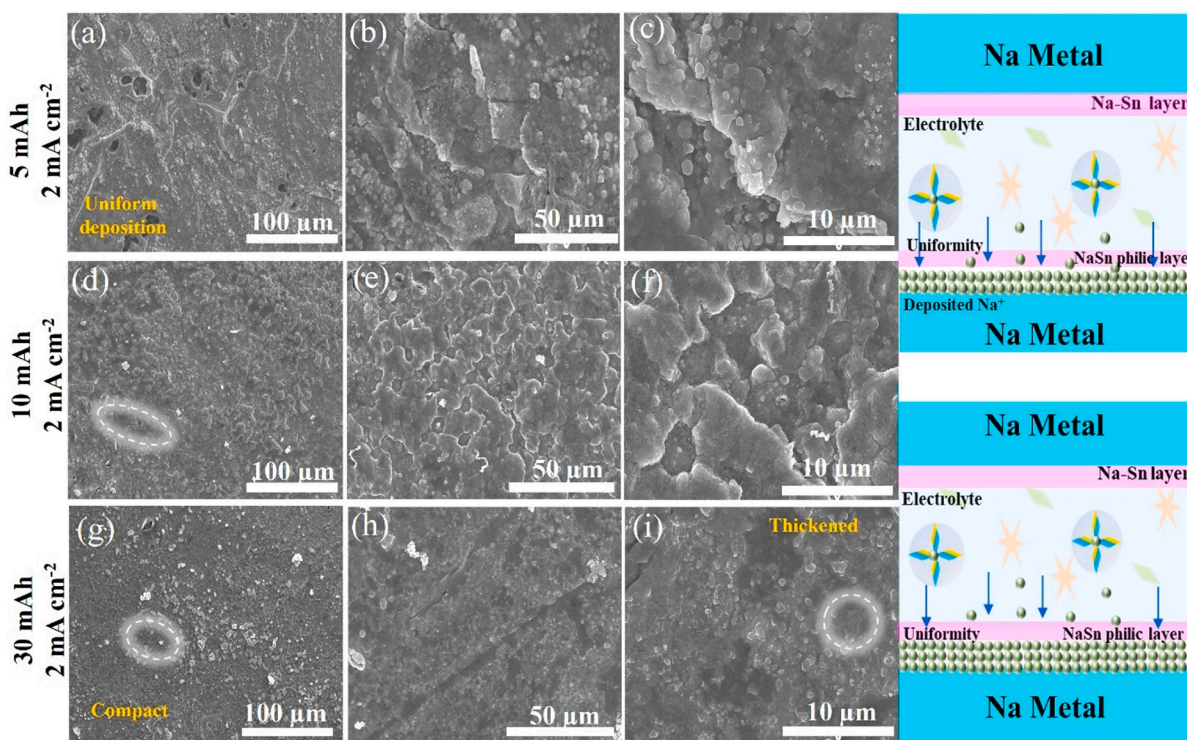


**Fig. 3.**  $\text{Na}^+$  deposition morphology evolution observed by SEM: (a–c) Top view of NS-a/NaF after sodium electrodeposition of  $5 \text{ mAh cm}^{-2}$  at  $2 \text{ mA cm}^{-2}$ . (d–f) Electrodeposition of  $10 \text{ mAh cm}^{-2}$  at  $2 \text{ mA cm}^{-2}$ . (g–i) Electrodeposition of  $30 \text{ mAh cm}^{-2}$  at  $2 \text{ mA cm}^{-2}$  using  $1 \text{ M NaPF}_6$  in diglyme electrolyte. All electrodes underwent  $\text{Na}^+$  deposition for 25 cycles prior to SEM analysis.

identical conditions reveals significant roughness and irregularities. At a lower areal capacity of  $5 \text{ mAh cm}^{-2}$ , the sodium metal surface begins to exhibit small grooves, indicating early signs of surface instability in deposition/stripping during continuous cycling. This behavior is attributed to the presence of a thin, predominantly organic SEI layer, which provides limited regulation of  $\text{Na}^+$  flux and fails to maintain long-term interfacial stability. As the areal capacity increases to  $10 \text{ mAh cm}^{-2}$ , localized dendritic features such as tiny dendrites and ridge-like structures become more evident, resulting again inhomogeneous  $\text{Na}^+$  deposition. These issues become more pronounced at higher capacities, especially  $10$  and  $30 \text{ mAh cm}^{-2}$ , where agglomerated, needle-like dendrites dominate the surface morphology (Fig. S8). This highlights the critical need for a robust interfacial design, because under prolonged cycling, the native SEI layer becomes unstable and eventually breaks down due to continuous mechanical stress and volume fluctuations. At worse, aggressive and sharp dendrite growth re-emerges, which poses the risk of piercing the separator, potentially leading to short circuits [60,61]. To visually capture the effectiveness of the NS-a/NaF artificial interphase in suppressing dendrite formation and pristine Na with dendrites, in situ optical microscopy was employed. For this analysis, transparent cuvette cells were fabricated, by filling them with electrolyte and placed pristine sodium electrodes on both sides, including the modified sodium anodes (NS-a/NaF). In these symmetric cells, galvanostatic  $\text{Na}^+$  deposition was performed at a current density of  $1 \text{ mA cm}^{-2}$  for 0 min to 1 hour to observe the sodium dendrite evolution. (Fig. S9). At the initial stage, both the pristine Na and the NS-a/NaF electrodes exhibited smooth and clean surfaces without any observable disruption. However, after 30 min of deposition, the pristine Na electrode began to show inhomogeneous  $\text{Na}^+$  deposition on the surface (Fig. 4a). With continued deposition, mossy-type sodium deposits and small dendritic structures started to emerge. Eventually, some regions were covered with dead sodium, while in other areas, dominated by sharp needle-like dendrites as highlighted. These dendrites promote a tip effect, where incoming  $\text{Na}^+$  ions tend to deposit at the tips of existing structures due to

localized high ion concentrations. This kind of behavior reduces Coulombic efficiency and, in worst cases, can lead to short circuits or trigger cell failure. In contrast, NS-a/NaF-modified electrodes displayed a markedly different behavior.  $\text{Na}^+$  ions deposited uniformly across the surface, maintaining a smooth, flat, and compact texture even after extended deposition times. This improved morphology is attributed to the high ionic conductivity and partial insulating nature of the NS-a/NaF interphase, which facilitates  $\text{Na}^+$  diffusion beneath the surface and promotes homogeneous deposition. Throughout the entire deposition process, the NS-a/NaF electrode remained stable and free of visible disruptions. These results clearly highlight the stark contrast between pristine Na, NS-a/NaF interphases and also strongly indicate that the NS-a/NaF interphase effectively suppresses dendritic sodium.

Then, XPS analysis was conducted on cycled NS-a/NaF electrodes to assess the chemical/electrochemical stability of the artificial interphase after repeated cycling. After 10 and 50 plating/stripping cycles, the symmetric cells were disassembled in an argon-filled glove box, and the electrodes were gently rinsed to remove residual electrolyte (Fig. 4b). The Na 1s peak at  $1071.1 \text{ eV}$  corresponds to the  $\text{Na}_{15}\text{Sn}_4$  phase, confirming the formation of a sodio-philic conducting alloy within the interfacial layer. Similarly, metallic Sn peaks observed at  $486.3 \text{ eV}$  and Na–Sn alloy phases observed at  $485.8 \text{ eV}$ , while the F 1s peak at  $684.3 \text{ eV}$  verifies the retention of NaF. Notably, these spectra exhibit no significant deviation from the initially formed interphase layer, indicating excellent chemical stability of the  $\text{Na}_{15}\text{Sn}_4\text{NaF}$  interphase [62,63]. However, after 50 cycles, a slight shift in the Na 1s binding energy is observed ( $1076.2 \text{ eV}$ ), which can be attributed to partial oxidation of the sodium surface during sample transfer. In the case of the Sn 3d and F 1s spectra, the peaks shift slightly toward lower and higher binding energies, because of electrochemical cycling (Fig. 4c).

Additionally, to validate the enhanced electrochemical performance of the NS-a/NaF SEI interphase over pristine Na metal, symmetric cell tests were performed under varying current densities and areal capacities. As predicted by Sand's classical theory (1901), increasing the

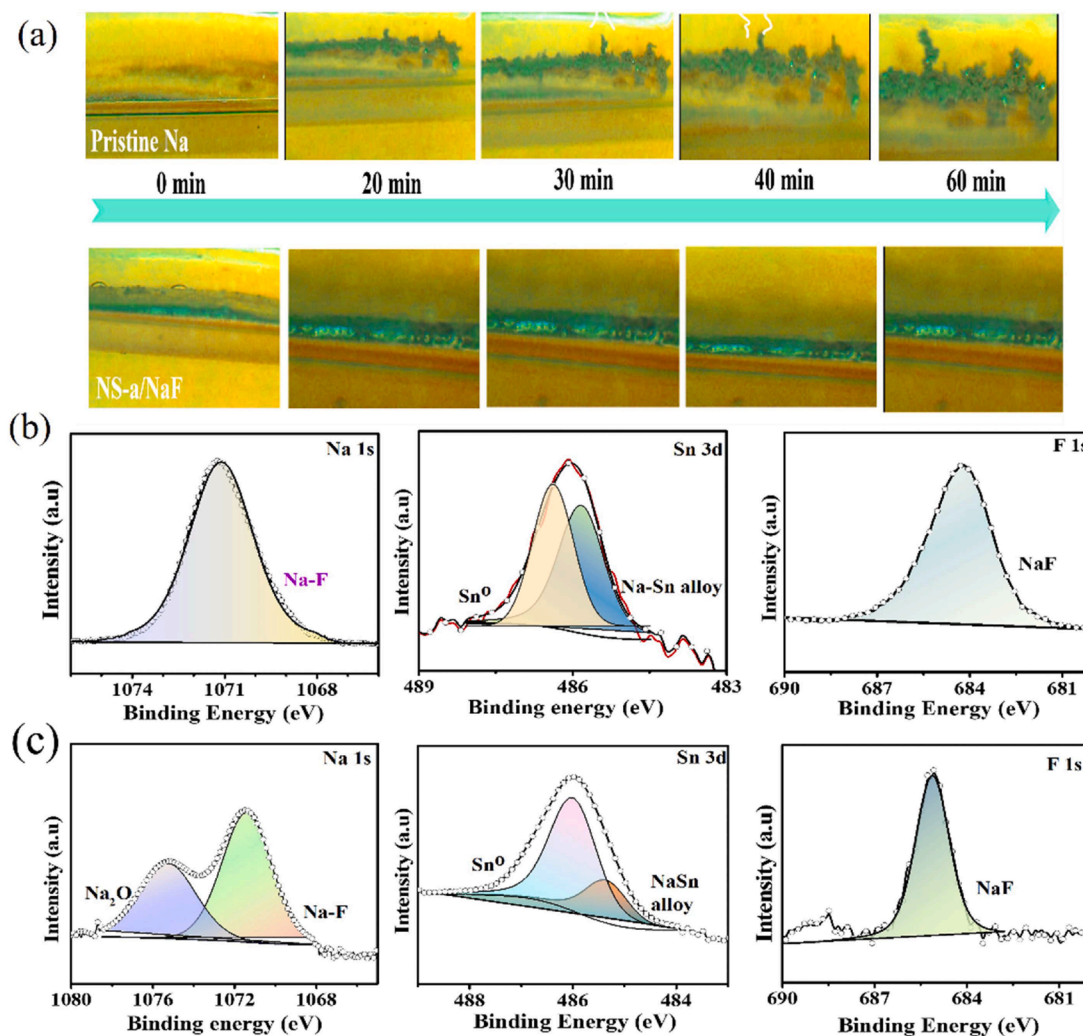
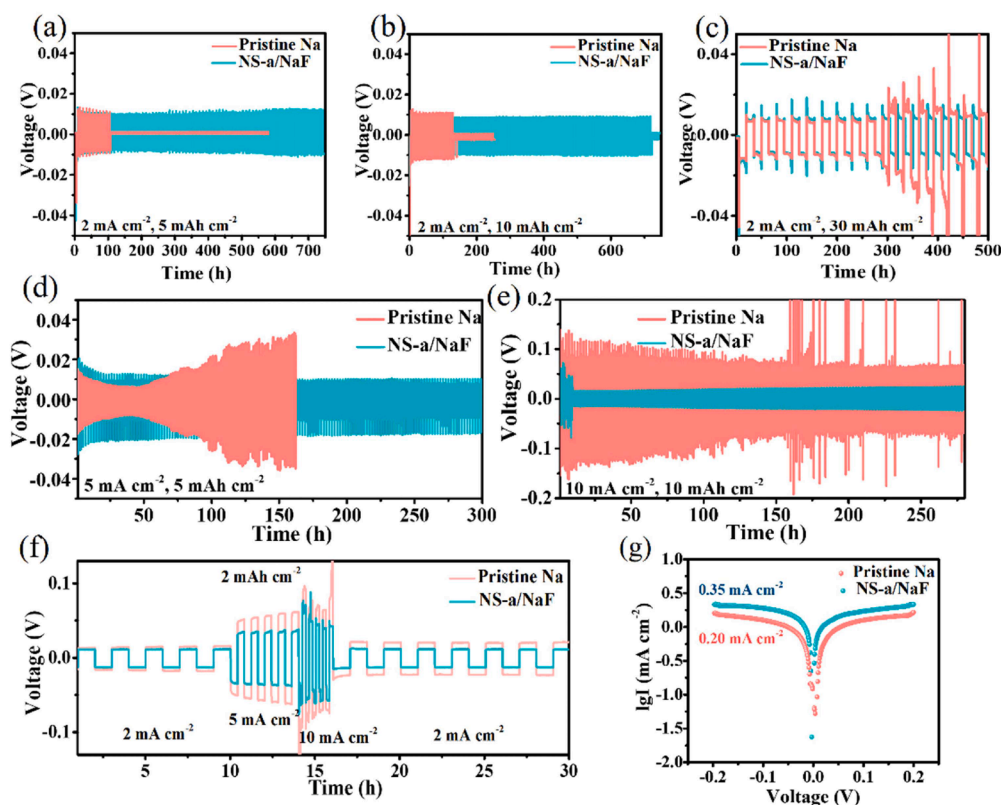


Fig. 4. a) Optical microscopy images showing dendrite formation on pristine Na and smooth interphase on NS-a/NaF electrodes. b) XPS peak fitting of the NS-a/NaF electrodes after 10 cycles c) after 50 cycles, respectively.

current density and areal capacity can lead to pronounced dendrite formation. Therefore, both current density and deposition time were systematically optimized and investigated [64]. As shown in (Fig. 5a), when the current density kept  $2 \text{ mA cm}^{-2}$ , areal capacity is  $5 \text{ mAh cm}^{-2}$  the NS-a/NaF anode maintained uniform plating/stripping behavior for up to 748 h with an overpotential of 17 mV, while the pristine Na metal exhibited a lifespan of only 105 h with a slightly higher overpotential of 22 mV, but the cell is dead. In the pristine Na anode, the naturally formed SEI layers lack the mechanical robustness, which are necessary to sustain large volumes, resulting in non-uniform sodium deposition [50]. As the areal capacity increased to  $10 \text{ mAh cm}^{-2}$ , the elevated sodium ion flux intensified the risk of dendrite formation caused by non-uniform deposition. This non-uniform sodium flux, combined with dendrite growth gives the lifespan about 129 h, critically affects the longevity, and safety of SMBs [65]. Conversely, the NS-a/NaF anode demonstrated stable performance, achieving a lifespan of up to 719 h of plating/stripping, more than twice that of pristine Na metal, with a consistent overpotential of 18 mV (Fig. 5b). Even when the areal capacity was increased to  $30 \text{ mAh cm}^{-2}$ , the NS-a/NaF anode maintained stable plating/stripping performance for up to 500 h with an overpotential of 21 mV, whereas the pristine Na metal remained stable only up to 250 h, with an overpotential of 30 mV and showing abrupt voltage fluctuations (Fig. 5c). After several cycles, the pristine Na metal anode failed, characterized by uneven plating/stripping. The non-uniform sodium deposition into the SEI interphase resulted in fragile,

nucleus-shaped structures that lacked the mechanical strength to endure stress, particularly under either high current or capacity conditions [66, 67]. At a moderate areal capacity of  $5 \text{ mAh cm}^{-2}$  and current density of  $5 \text{ mA cm}^{-2}$ , the NS-a/NaF symmetric cell exhibited stable cycling for up to 300 hours with smooth plating/stripping behavior as shown in (Fig. 5d). In contrast, the pristine Na electrode displayed an initial overpotential of  $\sim 30 \text{ mV}$ , which progressively increased during cycling and led to cell failure within a few hours. When subjected to even more extreme conditions  $10 \text{ mAh cm}^{-2}$  at  $10 \text{ mA cm}^{-2}$ , the pristine Na electrode maintained stable operation only before experiencing abrupt voltage drops, indicative of rapid dendrite formation and internal shorting. Once dendrites are formed, they critically undermine the battery's lifespan. In comparison, the NS-a/NaF electrode demonstrated superior stability, sustaining continuous cycling for over 281 hours with a moderate overpotential as shown in (Fig. 5e).

For the comparison purposes, other halogenated interface-based electrodes were tested at different areal capacity and same current density as shown in (Fig. S10). While these halogenated interphases offered improved stability relative to pristine Na, but their inferior mechanical strength limited their performance, falling short of durability than the NS-a/NaF-modified electrode. The superior electrochemical performance of the NS-a/NaF anode is further substantiated by rate performance studies using symmetric cells with both pristine Na and NS-a/NaF anodes. At varying current densities the NS-a/NaF anode maintains a stable voltage profile without any voltage spikes, whereas



**Fig. 5.** Symmetric cells and their voltage profiles under different sodium ion deposition conditions. a) 5 mAh cm<sup>-2</sup>, 2 mA cm<sup>-2</sup>. b) 10 mAh cm<sup>-2</sup>, 2 mA cm<sup>-2</sup>. c) 30 mAh cm<sup>-2</sup>, 2 mA cm<sup>-2</sup>. d) 5 mAh cm<sup>-2</sup>, 5 mA cm<sup>-2</sup>. e) 10 mAh cm<sup>-2</sup>, 10 mA cm<sup>-2</sup>. f) Rate performance. g) LSV plot for exchange current density determination.

the pristine Na metal experiences multiple voltage spikes under high reaction kinetics due to its inability to withstand sudden variations and stress as shown in (Fig. 5f) [68]. LSV curves reveal a higher exchange current density for the NS-a/NaF electrode ( $\sim 0.35$  mA cm<sup>-2</sup>) compared to pristine Na ( $\sim 0.20$  mA cm<sup>-2</sup>), indicating faster interfacial charge-transfer kinetics. This enhancement is attributed to the conductive Na<sub>15</sub>Sn<sub>4</sub> alloy and stable NaF-based SEI layer (Fig. 5g). The temperature-dependent EIS spectra shows that the NS-a/NaF anode exhibits significantly lower interfacial resistance compared to pristine Na at all temperatures. With increasing temperature, the impedance of NS-a/NaF drops more rapidly, indicating enhanced Na<sup>+</sup> ion transport even during the temperature variations as shown in (Fig. S11). This behavior highlights the superior ionic conductivity and thermal stability of the engineered interphase. Overall, the NS-a/NaF layer ensures efficient charge transfer and stable performance even under elevated temperatures.

To further validate the electrochemical performance of the NS-a/NaF modified anode for sodium metal batteries, a full cell was assembled using a NS-a/NaF anode and Na<sub>3</sub>V<sub>2</sub>(PO<sub>4</sub>)<sub>3</sub> (NVP) cathode, as schematically illustrated in (Fig. 6a). In the cyclic voltammetry (CV) of full cells, (Fig. S12), the peak current is higher for the NS-a/NaF || NVP cells compared to the pristine Na || NVP cells. The larger peak current indicates that the Na<sup>+</sup> diffusion kinetics are enhanced and better optimized in the modified system. Moreover, the oxidation and reduction peak potentials are closer in the NS-a/NaF anodes, suggesting a lower polarization voltage and improved electrochemical reversibility. The charge-discharge profiles at 1C rate (Fig. 6b & c) demonstrate that the NS-a/NaF/NVP full cell delivers a higher reversible discharge capacity (107 mAh g<sup>-1</sup>) compared to the pristine Na/NVP (100 mAh g<sup>-1</sup>). The polarization voltage of NS-a/NaF artificial interface/pristine Na is analyzed using GCD performance of both cells at 1C rate, after 50th cycles. Pristine Na/NVP cells polarization voltage is 0.074 V higher than NS-a/NaF anode of 0.067 V (Fig. S13). This clearly indicates that the

new interfaces have the improved diffusion kinetics, so that ions can easily diffuse and deposit beneath the SEI. Over extended cycling, the NS-a/NaF cell maintains superior capacity retention for over 200 cycles, while the pristine Na-based full cell exhibits a noticeable decline in Coulombic efficiency after 150 cycles (Fig. 6d). This degradation is attributed to the unstable and non-uniform native SEI, which fails to regulate homogeneous sodium deposition and promotes dendrite formation. Rate capability was further evaluated at various current densities ranging from 1C to 5C. The pristine Na/NVP full cell showed discharge capacities of 106, 102.2, 91, 77, 68, and 102.5 mAh g<sup>-1</sup> at 1C, 2C, 3C, 4C, 5C, and back to 1C, respectively. In contrast, the NS-a/NaF/NVP full cell exhibited improved rate performance with capacities of 110.5, 109.2, 98.3, 89.4, 81.0, and 110.2 mAh g<sup>-1</sup> at the corresponding rates (Fig. 6e). After 50 cycles, interfacial charge transfer resistance measurements were conducted to substantiate these findings. The pristine Na vs NVP full cell exhibited a high interphase resistance of 86.42 Ω, more than twice that of the NS-a/NaF anode, which showed a lower resistance of 33.10 Ω (Fig. 6f). This reduction is attributed to the engineered artificial SEI, which facilitates faster Na<sup>+</sup> diffusion and favorable electron modulation at the interface. The enhanced electrochemical performance of the NS-a/NaF interphase stems from its rationally engineered dual-phase structure, as schematically shown in (Fig. 6g). The Na<sub>15</sub>Sn<sub>4</sub> alloy provides excellent sodio-philicity and high ionic conductivity, enabling uniform Na<sup>+</sup> nucleation and fast ion transport, while the NaF phase, an electronic insulator with high mechanical strength, prevents electron leakage and inhibits dendrite penetration. Together, they form a homogeneous, robust SEI that ensures smooth Na plating/stripping, suppresses dendrite formation, and extends cycling life under high-rate conditions. In contrast, the pristine Na anode relying on a fragile, naturally formed SEI struggles to sustain high current densities and capacities, leading to instability and poor long-term performance.

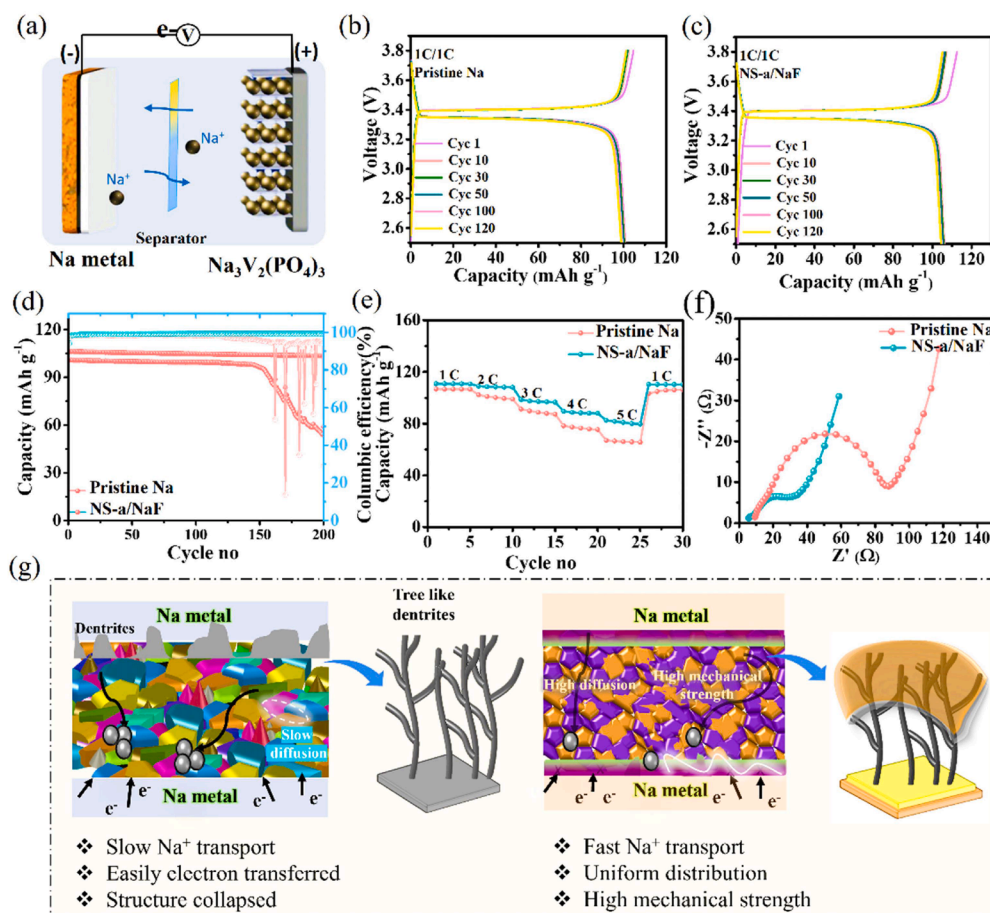


**Fig. 6.** a) Schematic diagram of the sodium metal battery. Electrochemical performance of a full cell. b) Charge–discharge profile of pristine Na vs. NVP. c) Charge–discharge profile of NS-a/NaF vs. NVP. d) Cycling stability at rate of 1C. e) Rate performance at different C-rates for both electrodes. f) EIS analysis after 50 cycles. g) Proposed working mechanism of natural and artificial interlayers on sodium metal anodes and their impact on battery performance.

#### 4. Conclusion

We have successfully designed a  $\text{Na}_{15}\text{Sn}_4$ -alloy/NaF interphase, that is both ionically conductive and mechanically robust, enabling exceptional cycling stability even at high current densities. The  $\text{Na}_{15}\text{Sn}_4$  alloy serves as a sodio-philic conducting scaffold, promoting uniform  $\text{Na}^+$  nucleation and facilitating smooth plating/stripping behavior. Simultaneously, the NaF component offers mechanical reinforcement and electronic insulation, effectively suppressing dendrite formation and parasitic side reactions. The (NS-a/NaF) interphase significantly reduces interfacial resistance and enhances  $\text{Na}^+$  ion transport, as demonstrated by symmetric cell operation exceeding 2000 hours and full-cell performance retaining  $110.15 \text{ mAh g}^{-1}$  at 1C over 200 cycles. These improvements were further corroborated by in situ optical microscopy and XPS analysis, confirming the structural and chemical stability of the interphase. This study presents a scalable and practical strategy for engineering multifunctional interphases, providing a promising pathway toward safe, high-rate, and long-life sodium metal batteries.

#### CRediT authorship contribution statement

**Megala Moorthy:** Writing – original draft, Methodology, Formal analysis, Data curation, Conceptualization. **Ranjith Thangavel:** Writing – review & editing, Methodology, Investigation, Formal analysis. **So Yeon An:** Data curation, Conceptualization. **Hariharan Dhanasekaran:** Data curation, Conceptualization. **Yun Sung Lee:** Writing – review & editing, Funding acquisition, Formal analysis, Data curation, Conceptualization.

#### Declaration of competing interest

The authors declare that they have no known competing financial interests or personal relationships that could have appeared to influence the work reported in this paper.

#### Acknowledgement

This work was financially supported by a National Research Foundation of Korea (NRF) grant funded by the Korean government (Ministry of Science, ICT & Future Planning) (No. RS-2021-NR057375). Dr. Ranjith Thangavel acknowledges the support from the CPRI, Bangalore under the Ministry of Power, Government of India, through NPP scheme (NPP/21-26/GD/4).

#### Supplementary materials

Supplementary material associated with this article can be found, in the online version, at [doi:10.1016/j.surfin.2025.108323](https://doi.org/10.1016/j.surfin.2025.108323).

#### Data availability

All the data supporting this study are available within the article and supplementary information

## References

- [1] V.S. Arunachalam, E.L. Fleischer, The global energy landscape and materials innovation, *MRS Bull.* 33 (2008) 264–288, <https://doi.org/10.1557/mrs2008.61>.
- [2] S.J. Lee, M. Moorthy, S. Park, Y.S. Lee, Enhanced nitrogen-doped reduced graphene oxide-embedded MnMoO<sub>4</sub> as high-capacity and stable anode for sodium-ion batteries, *J. Ind. Eng. Chem.* 131 (2024) 199–207, <https://doi.org/10.1016/j.jiec.2023.10.019>.
- [3] J. Chang Seol, R. Balasubramaniam, V. Aravindan, R. Thangavel, Y.S. Lee, Ameliorating the electrode/electrolyte interface compatibility in Li-ion solid-state batteries with plasticizer, *J. Alloys Compd.* 927 (2022) 167077, <https://doi.org/10.1016/j.jallcom.2022.167077>.
- [4] E. Matios, H. Wang, C. Wang, W. Li, Enabling safe sodium metal batteries by solid electrolyte interphase engineering: a review, *Ind. Eng. Chem. Res.* 58 (2019) 9758–9780, <https://doi.org/10.1021/acs.iecr.9b02029>.
- [5] Y. Wang, Y. Wang, Y.-X. Wang, X. Feng, W. Chen, X. Ai, H. Yang, Y. Cao, Developments and perspectives on emerging high-energy-density sodium-metal batteries, *Chem* 5 (2019) 2547–2570, <https://doi.org/10.1016/j.chempr.2019.05.026>.
- [6] R. Thangavel, D. Han, B. Moorthy, B. Krishnan Ganesan, Understanding the structural phase transitions in Na<sub>3</sub>V<sub>2</sub>PO<sub>4</sub> 3 symmetrical sodium-ion batteries using synchrotron-based X-ray techniques, *Small Methods* 6 (2022) 2100888, <https://doi.org/10.1002/smt.202100888>.
- [7] M. Moorthy, R. Thangavel, S. An, A. Anilkumar, D. Han, Recent trends in artificial SEI layers for controlling dendrite formation and enhancing cycle life : toward stable and durable sodium metal batteries, *Small* 21 (2025) 2502974, <https://doi.org/10.1002/sml.202502974>.
- [8] L. Ma, J. Cui, S. Yao, X. Liu, Y. Luo, X. Shen, J.K. Kim, Dendrite-free lithium metal and sodium metal batteries, *Energy Storage Mater.* 27 (2020) 522–554, <https://doi.org/10.1016/j.ensm.2019.12.014>.
- [9] M. Moorthy, R. Thangavel, B. Krishnan Ganesan, A. Saha, S. Hong, Y.S. Lee, Ultra-high areal capacity, ultra-long life, dendrite-free sodium metal anode enabled by antimony-based Na-ion conducting artificial SEI layers, *Chem. Eng. J.* 498 (2024) 155234, <https://doi.org/10.1016/j.cej.2024.155234>.
- [10] X. Xu, D. Zhou, X. Qin, K. Lin, F. Kang, B. Li, D. Shanmukaraj, T. Rojo, M. Armand, G. Wang, A room-temperature sodium–sulfur battery with high capacity and stable cycling performance, *Nat. Commun.* 9 (2018) 1–12, <https://doi.org/10.1038/s41467-018-06443-3>.
- [11] Y. Yao, Z. Wei, H. Wang, H. Huang, Y. Jiang, X. Wu, X. Yao, Z.S. Wu, Y. Yu, Toward high energy density all solid-state sodium batteries with excellent flexibility, *Adv. Energy Mater.* 10 (2020) 1903698, <https://doi.org/10.1002/aenm.201903698>.
- [12] H. Yadegari, Q. Sun, X. Sun, Sodium-oxygen batteries: a comparative review from chemical and electrochemical fundamentals to future perspective, *Adv. Mater.* 28 (2016) 7065–7093, <https://doi.org/10.1002/adma.201504373>.
- [13] X. Hu, J. Sun, Z. Li, Q. Zhao, C. Chen, J. Chen, Rechargeable room-temperature Na-CO<sub>2</sub> batteries, *Angew. Chem. Int. Ed.* 55 (2016) 6482–6486, <https://doi.org/10.1002/anie.201602504>.
- [14] X. Lv, F. Tang, Y. Yao, C. Xu, D. Chen, L. Liu, Y. Feng, X. Rui, Y. Yu, Sodium–gallium alloy layer for fast and reversible sodium deposition, *SusMat* 2 (2022) 699–707, <https://doi.org/10.1002/sus2.97>.
- [15] H. Shi, Y. Zhang, Y. Liu, C. Yuan, Metallic sodium anodes for advanced sodium metal batteries: progress, challenges and perspective, *Chem. Rec.* 22 (2022) e202200112, <https://doi.org/10.1002/tcr.202200112>.
- [16] G. Yang, N. Li, C. Sun, High-performance sodium metal batteries with sodium-bismuth alloy anode, *ACS Appl. Energy Mater.* 3 (2020) 12607–12612, <https://doi.org/10.1021/acsaem.0c02510>.
- [17] X. Wang, J. Lu, Y. Wu, W. Zheng, H. Zhang, T. Bai, H. Liu, D. Li, L. Ci, Building stable anodes for high-rate Na-metal batteries, *Adv. Mater.* 36 (2024) 2311256, <https://doi.org/10.1002/adma.202311256>.
- [18] W.S. Xiong, Y. Jiang, Y. Xia, Y. Qi, W. Sun, D. He, Y. Liu, X.Z. Zhao, A robust 3D host for sodium metal anodes with excellent machinability and cycling stability, *Chem. Commun.* 54 (2018) 9406–9409, <https://doi.org/10.1039/c8cc03996h>.
- [19] C. Chen, W. Yao, Y. Tang, Emerging solutions to enable the efficient use of sodium metal anodes: progress and perspectives, *Adv. Funct. Mater.* 34 (2024) 2310833, <https://doi.org/10.1002/adfm.202310833>.
- [20] T. Liu, Z. Yang, Y. Tang, J. Liu, Y. Ma, Promoting the cation utilization in energy-dense sodium metal battery prototypes: strategies, analysis, and prospects, *Small Sci.* 4 (2024) 2300108, <https://doi.org/10.1002/sssc.202300108>.
- [21] T. Ma, L. Zhang, Y. Tan, P. Zhou, X. Liu, A. Tian, C. Wang, Y. Wu, W. Ding, Y. Yang, F. Liu, Multiscale free-standing graphene-based scaffolds enabling advanced high-energy and dendrite-free lithium metal anodes, *J. Energy Storage* 93 (2024) 112283, <https://doi.org/10.1016/j.est.2024.112283>.
- [22] F. Liu, P. Zuo, J. Li, P. Shi, Y. Shao, L. Chen, Y. Tan, T. Ma, A layered multifunctional framework based on polyacrylonitrile and MOF derivatives for stable lithium metal anode, *J. Energy Chem.* 93 (2024) 282–288, <https://doi.org/10.1016/j.jechem.2024.02.014>.
- [23] B. Moorthy, S. Kwon, J.H. Kim, P. Ragupathy, H.M. Lee, D.K. Kim, Tin sulfide modified separator as an efficient polysulfide trapper for stable cycling performance in Li-S batteries, *Nanoscale Horizons* 4 (2019) 214–222, <https://doi.org/10.1039/c8nh00172c>.
- [24] B. Moorthy, R. Ponraj, J.H. Yun, J.E. Wang, D.J. Kim, D.K. Kim, Ice-templated free-standing reduced graphene oxide for dendrite-free lithium metal batteries, *ACS Appl. Energy Mater.* 3 (2020) 11053–11060, <https://doi.org/10.1021/acsaem.0c01946>.
- [25] B. Moorthy, J.H. Kim, H.W. Lee, D.K. Kim, Vertically aligned carbon nanotubular structure for guiding uniform lithium deposition via capillary pressure as stable metallic lithium anodes, *Energy Storage Mater.* 24 (2020) 602–609, <https://doi.org/10.1016/j.ensm.2019.06.016>.
- [26] J. Zhang, W. Wang, R. Shi, W. Wang, S. Wang, F. Kang, B. Li, Three-dimensional carbon felt host for stable sodium metal anode, *Carbon* N. Y. 155 (2019) 50–55, <https://doi.org/10.1016/j.carbon.2019.08.050>.
- [27] W. Go, M.H. Kim, J. Park, C.H. Lim, S.H. Joo, Y. Kim, H.W. Lee, Nanocrevase-rich carbon fibers for stable lithium and sodium metal anodes, *Nano Lett.* 19 (2019) 1504–1511, <https://doi.org/10.1021/acs.nanolett.8b04106>.
- [28] Z. Xu, J. Yang, T. Zhang, L. Sun, Y. Nuli, J. Wang, S. ichi Hirano, Stable Na metal anode enabled by a reinforced multistructural SEI layer, *Adv. Funct. Mater.* 29 (2019) 1901924, <https://doi.org/10.1002/adfm.201901924>.
- [29] P. Shi, S. Zhang, G. Lu, L. Wang, Y. Jiang, F. Liu, Y. Yao, H. Yang, M. Ma, S. Ye, X. Tao, Y. Feng, X. Wu, X. Rui, Y. Yu, Red Phosphorous-derived protective layers with high ionic conductivity and mechanical strength on dendrite-free sodium and potassium metal anodes, *Adv. Energy Mater.* 11 (2021) 2003381, <https://doi.org/10.1002/aenm.202003381>.
- [30] M. Xu, Y. Li, M. Ihsan-Ul-Haq, N. Mubarak, Z. Liu, J. Wu, Z. Luo, J.K. Kim, NaF-rich solid electrolyte interphase for dendrite-free sodium metal batteries, *Energy Storage Mater.* 44 (2022) 477–486, <https://doi.org/10.1016/j.ensm.2021.10.038>.
- [31] L. Xia, K. Li, Y. Zhang, H. Wu, Z. Fang, X. Yan, B. Sa, L. Wang, L. Lin, J. Lin, G. Wei, D.L. Peng, Q. Xie, Multiphase artificial interphase layer enabled long-life and dendrite-free sodium metal batteries, *J. Mater. Chem. A* 12 (2024) 17222–17228, <https://doi.org/10.1039/d4ta02925a>.
- [32] W. Zhao, M. Guo, Z. Zuo, X. Zhao, H. Dou, Y. Zhang, S. Li, Z. Wu, Y. Shi, Z. Ma, X. Yang, Engineering sodium metal anode with sodiophilic bismuthide penetration for dendrite-free and high-rate sodium-ion battery, *Engineering* 11 (2022) 87–94, <https://doi.org/10.1016/j.eng.2021.08.028>.
- [33] Z. Luo, S. Tao, Y. Tian, L. Xu, Y. Wang, X. Cao, Y. Wang, W. Deng, G. Zou, H. Liu, H. Hou, X. Ji, Robust artificial interlayer for columnar sodium metal anode, *Nano Energy* 97 (2022) 107203, <https://doi.org/10.1016/j.nanoen.2022.107203>.
- [34] K. Chen, H. Huang, S. Xu, Z. Yuan, Y. Yang, Y. Yao, X. Zhang, X. Rui, Y. Yu, Durable sodium iodide interphase stabilizing sodium metal anodes, *Carbon Neutrality* 3 (2024), <https://doi.org/10.1007/s43979-024-00082-y>.
- [35] M. Ali, S. Iqbal, A.N. Chishti, M. Ali, S. Aman, H. Hussain, Y. Jiang, X. Lin, M. Yousaf, A multifunctional ex-situ artificial hybrid interphase layer to stabilize sodium metal anode, *Nano Energy* 132 (2024) 110348, <https://doi.org/10.1016/j.nanoen.2024.110348>.
- [36] Y. Li, H. Dong, K. Xu, M. Chu, X. Xu, W. Zhao, Y. Xue, Q. Li, Y. Tan, C. Sun, L. Cao, H. Wei, H. Geng, Grain-boundary engineering of Na<sub>3</sub>Bi/NaF dual-functional heterogeneous protective layer for highly stable sodium metal anodes, *Energy Storage Mater.* 73 (2024) 103846, <https://doi.org/10.1016/j.ensm.2024.103846>.
- [37] Y. Cheng, X. Yang, M. Li, X. Li, X. Lu, D. Wu, B. Han, Q. Zhang, Y. Zhu, M. Gu, Enabling ultra-stable alkali metal anodes by artificial solid electrolyte interphase fluorination, *Nano Lett.* 22 (2022) 4347–4353, <https://doi.org/10.1021/acs.nanolett.2c00616>.
- [38] R.S. Kalubarme, J.Y. Lee, C.J. Park, Carbon encapsulated tin oxide nanocomposites: an efficient anode for high performance sodium-ion batteries, *ACS Appl. Mater. Interfaces* 7 (2015) 17226–17237, <https://doi.org/10.1021/acsaami.5b04178>.
- [39] S. Wu, Y. Qiao, K. Jiang, Y. He, S. Guo, H. Zhou, Tailoring sodium anodes for stable sodium–oxygen batteries, *Adv. Funct. Mater.* 28 (2018) 1706374, <https://doi.org/10.1002/adfm.201706374>.
- [40] J. Liu, S. Wang, K. Kravchik, M. Ibáñez, F. Krumeich, R. Widmer, D. Nasiou, M. Meyns, J. Llorca, J. Arbiol, M.V. Kovalenko, A. Cabot, Sn nanocrystals as anode materials for Na-ion batteries, *J. Mater. Chem. A* 6 (2018) 10958–10966, <https://doi.org/10.1039/c8ta01492b>.
- [41] M.K. Aslam, Y. Niu, T. Hussain, H. Tabassum, W. Tang, M. Xu, R. Ahuja, How to avoid dendrite formation in metal batteries: innovative strategies for dendrite suppression, *Nano Energy* 86 (2021) 106142, <https://doi.org/10.1016/j.nanoen.2021.106142>.
- [42] L. Cao, J. Guo, Y. Feng, Y. Li, Y. Qiu, W. Zhu, Y. Tan, C. Sun, X. Rui, H. Geng, A rooted multifunctional heterogeneous interphase layer enabled by surface-reconstruction for highly durable sodium metal anodes, *Adv. Funct. Mater.* 34 (2024) 2313962, <https://doi.org/10.1002/adfm.202313962>.
- [43] V. Kumar, Y. Wang, A.Y.S. Eng, M.F. Ng, Z.W. Seh, A biphasic interphase design enabling high performance in room temperature sodium-sulfur batteries, *Cell Rep. Phys. Sci.* 1 (2020) 100044, <https://doi.org/10.1016/j.xcrp.2020.100044>.
- [44] K. Thanner, A. Varzi, D. Buchholz, S.J. Sedlmaier, S. Passerini, Artificial solid electrolyte interphases for lithium metal electrodes by wet processing: the role of metal salt concentration and solvent choice, *ACS Appl. Mater. Interfaces* 12 (2020) 32851–32862, <https://doi.org/10.1021/acsaami.0c08938>.
- [45] X. Zhou, F. Liu, Y. Wang, Y. Yao, Y. Shao, X. Rui, F. Wu, Y. Yu, Heterogeneous interfacial layers derived from the in situ reaction of CoF<sub>2</sub> nanoparticles with sodium metal for dendrite-free Na metal anodes, *Adv. Energy Mater.* 12 (2022) 2202323, <https://doi.org/10.1002/aenm.202202323>.
- [46] M. Zhu, L. Li, Y. Zhang, K. Wu, F. Yu, Z. Huang, G. Wang, J. Li, L. Wen, H.K. Liu, S. X. Dou, Y. Yu, C. Wu, An in-situ formed stable interface layer for high-performance sodium metal anode in a non-flammable electrolyte, *Energy Storage Mater.* 42 (2021) 145–153, <https://doi.org/10.1016/j.ensm.2021.07.012>.
- [47] Z. Luo, S. Tao, Y. Tian, L. Xu, Y. Wang, X. Cao, Y. Wang, W. Deng, G. Zou, H. Liu, H. Hou, X. Ji, Robust artificial interlayer for columnar sodium metal anode, *Nano Energy* 97 (2022) 107203, <https://doi.org/10.1016/j.nanoen.2022.107203>.
- [48] Q. Shi, Y. Zhong, M. Wu, H. Wang, H. Wang, High-performance sodium metal anodes enabled by a bifunctional potassium salt, *Angew. Chem.* 130 (2018) 9207–9210, <https://doi.org/10.1002/ange.201803049>.

- [49] H. Wang, C. Wang, E. Matios, W. Li, Critical role of ultrathin graphene films with tunable thickness in enabling highly stable sodium metal anodes, *Nano Lett.* 17 (2017) 6808–6815, <https://doi.org/10.1021/acs.nanolett.7b03071>.
- [50] M. Moorthy, B. Moorthy, B.K. Ganesan, A. Saha, S. Yu, D.H. Kim, S. Hong, S. Park, K. Kang, R. Thangavel, Y.S. Lee, A series of hybrid multifunctional interfaces as artificial SEI layer for realizing dendrite free, and long-life sodium metal anodes, *Adv. Funct. Mater.* 33 (2023) 2300135, <https://doi.org/10.1002/adfm.202300135>.
- [51] Y. Zhao, L.V. Goncharova, Q. Zhang, P. Kaghazchi, Q. Sun, A. Lushington, B. Wang, R. Li, X. Sun, Inorganic-organic coating via molecular layer deposition enables long life sodium metal anode, *Nano Lett.* 17 (2017) 5653–5659, <https://doi.org/10.1021/acs.nanolett.7b02464>.
- [52] W. Luo, C.F. Lin, O. Zhao, M. Noked, Y. Zhang, G.W. Rubloff, L. Hu, Ultrathin surface coating enables the stable sodium metal anode, *Adv. Energy Mater.* 7 (2017) 1601526, <https://doi.org/10.1002/aenm.201601526>.
- [53] Y. Zhao, X. Yang, L.Y. Kuo, P. Kaghazchi, Q. Sun, J. Liang, B. Wang, A. Lushington, R. Li, H. Zhang, X. Sun, High Capacity, Dendrite-free growth, and minimum volume change Na metal anode, *Small* 14 (2018) 1703717, <https://doi.org/10.1002/smll.201703717>.
- [54] K. Cao, Y. Xia, H. Li, H. Huang, S. Iqbal, M. Yousaf, B. Bin Xu, W. Sun, M. Yan, H. Pan, Y. Jiang, Oxygen-regulated spontaneous solid electrolyte interphase enabling ultra-stable solid-state Na metal batteries, *Sci. Bull.* 69 (2024) 49–58, <https://doi.org/10.1016/j.scib.2023.11.017>.
- [55] A. Wang, X. Hu, H. Tang, C. Zhang, S. Liu, Y.W. Yang, Q.H. Yang, J. Luo, Processable and moldable sodium-metal anodes, *Angew. Chem. Int. Ed.* 56 (2017) 11921–11926, <https://doi.org/10.1002/anie.201703937>.
- [56] C. Wang, Y. Zheng, Z.N. Chen, R. Zhang, W. He, K. Li, S. Yan, J. Cui, X. Fang, J. Yan, G. Xu, D. Peng, B. Ren, N. Zheng, Robust anode-free sodium metal batteries enabled by artificial sodium formate interface, *Adv. Energy Mater.* 13 (2023) 2204125, <https://doi.org/10.1002/aenm.202204125>.
- [57] K. Yao, S. Xu, Y. Yang, Y. Zheng, K. Zuraqi, D. Yang, J. Liu, U. Mani, X. Rui, Designing sodium alloys for dendrite-free sodium-metal batteries, *Inf. Funct. Mater.* 1 (2024) 242–263, <https://doi.org/10.1002/ifm2.22>.
- [58] D. Li, Y. Sun, M. Li, X. Cheng, Y. Yao, F. Huang, S. Jiao, M. Gu, X. Rui, Z. Ali, C. Ma, Z.S. Wu, Y. Yu, Rational design of an artificial SEI: alloy/solid electrolyte hybrid layer for a highly reversible Na and K metal anode, *ACS Nano* 16 (2022) 16966–16975, <https://doi.org/10.1021/acs.nano.2c07049>.
- [59] X. Xia, C.F. Du, S. Zhong, Y. Jiang, H. Yu, W. Sun, H. Pan, X. Rui, Y. Yu, Homogeneous Na deposition enabling high-energy Na-metal batteries, *Adv. Funct. Mater.* 32 (2022) 2110280, <https://doi.org/10.1002/adfm.202110280>.
- [60] M. Jäckle, A. Groß, Microscopic properties of lithium, sodium, and magnesium battery anode materials related to possible dendrite growth, *J. Chem. Phys.* 141 (2014) 174710, <https://doi.org/10.1063/1.4901055>.
- [61] B. Lee, E. Paek, D. Mitlin, S.W. Lee, Sodium metal anodes: emerging solutions to dendrite growth, *Chem. Rev.* 119 (2019) 5416–5460, <https://doi.org/10.1021/acs.chemrev.8b00642>.
- [62] L. Baggetto, P. Ganesh, R.P. Meisner, R.R. Unocic, J.C. Jumas, C.A. Bridges, G. M. Veith, Characterization of sodium ion electrochemical reaction with tin anodes: experiment and theory, *J. Power Sources* 234 (2013) 48–59, <https://doi.org/10.1016/j.jpowsour.2013.01.083>.
- [63] X. Liang, Q. Pang, I.R. Kochetkov, M.S. Sempere, H. Huang, X. Sun, L.F. Nazar, A facile surface chemistry route to a stabilized lithium metal anode, *Nat. Energy* 2 (2017) 1–7, <https://doi.org/10.1038/nenergy.2017.119>.
- [64] H.S. Sand, On the concentration at the electrodes in a solution, with special reference to the liberation of hydrogen by electrolysis of a mixture of copper sulphate and sulphuric acid, *Proc. Phys. Soc. London* 17 (1899) 496–534, <https://doi.org/10.1088/1478-7814/17/1/332>.
- [65] G. Li, X. Lou, C. Peng, C. Liu, W. Chen, Interface chemistry for sodium metal anodes/batteries: a review, *Chem. Synth.* 2 (2022) 16, <https://doi.org/10.20517/cs.2022.19>.
- [66] D. Luo, L. Zheng, Z. Zhang, M. Li, Z. Chen, R. Cui, Y. Shen, G. Li, R. Feng, S. Zhang, G. Jiang, L. Chen, A. Yu, X. Wang, Constructing multifunctional solid electrolyte interface via in-situ polymerization for dendrite-free and low N/P ratio lithium metal batteries, *Nat. Commun.* 12 (2021) 1–11, <https://doi.org/10.1038/s41467-020-20339-1>.
- [67] Q. Jin, H. Lu, Z. Zhang, J. Xu, B. Sun, Y. Jin, K. Jiang, Synergistic manipulation of Na<sup>+</sup> flux and surface-preferred effect enabling high-areal-capacity and dendrite-free sodium metal battery, *Adv. Sci.* 9 (2022), <https://doi.org/10.1002/advs.202103845>.
- [68] J. Xie, Z. Li, X. Zheng, F. Tian, D. Lei, C. Wang, Built-in electric field of in situ formed artificial interface layer induces fast and uniform sodium-ions transmission to achieve a long-term stable sodium metal battery under harsh conditions, *Adv. Funct. Mater.* (2024), <https://doi.org/10.1002/adfm.202315309>.